Article

Not peer-reviewed version

A Facile Two-Step Thermal Process for Producing Dense Phase Pure Cubic Ta-Doped Lithium Lanthanum Zirconium Oxide Electrolyte for Upscaling

Diwakar Karuppiah , Dmitrii Komissarenko , Nur Sena Yuzbasi , Yang Liu ,
Pradeep Vallachira Warriam Sasikumar , Amir Hadian , Thomas Graule , Frank Clemens , Gurdial Blugan *

Posted Date: 18 October 2023

doi: 10.20944/preprints202310.1065.v1

Keywords: solid electrolyte; lithium batteries; LLZO, solid state batteries, lithium metal

doi:10.20944/preprints202310.1065.v1

Article

A Facile Two-Step Thermal Process for Producing Dense Phase Pure Cubic Ta-Doped Lithium Lanthanum Zirconium Oxide Electrolyte for Upscaling

Diwakar Karuppiah [1,2,*], Dmitrii Komissarenko [1,3], Nur Sena Yüzbasi [1], Yang Liu [1], Pradeep Vallachira Warriam Sasikumar [1,4], Amir Hadian [1,3], Thomas Graule, Frank Clemens [1] and Gurdial Blugan [1,*]

[1] Laboratory for High-Performance Ceramics, Empa, Swiss Federal Laboratories for Materials Science and Technology, CH-8600, Dübendorf, Switzerland
[2] Department of Mechanical Engineering Applied Mechanics, University of Pennsylvania, Philadelphia, PA 19104, USA
[3] University of Applied Sciences and Arts Northwestern Switzerland (FHNW), CH-5210 Windisch, Switzerland
[4] ADVANO, Lakeshore Drive, New Orleans, LA 70112, USA
* Correspondence: diwakarkaruppiah92@gmail.com and gurdial.blugan@empa.ch

Abstract: An inorganic solid electrolyte is the most favorable candidate for replacing flammable liquid electrolytes in lithium batteries. Lithium Lanthanum Zirconium Oxide (LLZO) is considered as a promising solid electrolyte due to its safe operating potential window (0-5V) combined with its good electrochemical stability. In this work, 250 g batches of pre-sintered Ta-doped ($Li_7La_3Zr_{1.6}Ta_{0.4}O_{12}$, Ta-LLZO) were synthesized for bulk production of dense LLZO electrolyte. A simple two-step thermal treatment process was developed. The first thermal step at 950 °C initiates nucleation of LLZO carefully controlling process parameters such as heating atmosphere, temperature and dopant concentration. In the second thermal step at 1150 °C, sintered discs were obtained as solid electrolytes, with relative densities of 96%. X-ray diffraction analysis confirmed the phase purity of the sintered Ta-LLZO disc, and refined data was used to calculate the lattice parameter (12.944 Å). Furthermore, the presence of the Ta dopant in the disc was confirmed through X-ray photoelectron spectroscopy (XPS) analysis. The ionic and electronic conductivity values of Ta-LLZO disc were 10^{-4} S cm^{-1} and 10^{-10} S cm^{-1}, respectively. These values confirm that the prepared (Ta-LLZO) discs exhibit ionic conductivity while being electronically insulating, being suitable for use as solid electrolytes with the requisite electrical properties.

Keywords: solid electrolyte; lithium batteries; LLZO, solid state batteries, lithium metal

1. Introduction

$Li_7La_3Zr_2O_{12}$ (LLZO) is one of the most promising inorganic solid electrolytes for lithium batteries due to its high melting point, ionic conductivity, chemical stability, and wide electrical potential window (0 to 5V) with respect to lithium [1]. LLZO exists in two different crystalline phases, cubic and tetragonal. The cubic phase (*c*-LLZO) with high ionic conductivity (10^{-3} S cm^{-1}) is preferred over the tetragonal (*t*-LLZO) phase with its lower conductivity (10^{-6} S cm^{-1}). The starting component powders are oxidized at temperatures exceeding>1000 °C to form LLZO. It is noteworthy that the cubic phase predominates at higher temperatures. However, upon cooling to room temperature, the tetragonal phase becomes more prominent. Stabilizing the cubic phase at room temperature is crucial; this is often achieved through the addition of cations. Hence, the incorporation of different cations to replace the existing ones, such as Li^+, La^{3+} and Zr^{4+}, in the crystal lattice of LLZO [2,3] is employed to address this challenge. The second important challenge is producing solid LLZO electrolytes with high density. Achieving low porosity in LLZO is essential to limit undesired lithium dendrite growth, which can lead to short circuiting. To achieve this, high temperatures (>1000 °C) and prolonged dwell times are often utilized. Therefore, various thermal treatments, such as spark plasma sintering [4], flash sintering [5], field-assisted sintering [6], oscillatory pressure sintering [7], hot-press sintering [8], and solid-state reaction (SSR) [9] have been widely investigated to achieve high density LLZO.

Among these methods, SSR stands out as a cost-effective approach, despite its limitations such as lithium loss and undesired formation of the tetragonal phase due to high temperatures and prolonged dwell times. To address this issue, large amounts of mother powder (powder bed) are consumed during the process. The cost of mother powder is high, mainly due to the lithium precursor. To compensate for lithium loss, excess lithium salt (precursor) can be utilized [10–12].

In addition to this, the choice of crucibles used during synthesis plays a significant role. Jiang et al. [13] investigated the influence of sintering crucibles on phase purity of Ta-LLZO (specifically MgO and Al_2O_3 crucibles) when the lid is used. Their study demonstrated that MgO is the most suitable candidate for synthesis of *c*-LLZO over Al_2O_3, owing to its enhanced chemical inertness at elevated temperatures [14–17].

Furthermore, numerous studies have employed various methodologies to synthesize *c*-LLZO [18–20]. However, upscaling of LLZO production using these known synthesis methods can be challenging. Therefore, development of a methodology with the necessary process steps to enable repeatable production in large batch sizes is crucial as a first step.

In this study, 250 grams of pre-sintered LLZO ($Li_7La_3Zr_{1.6}Ta_{0.4}O_{12}$) powder per batch were synthesized via SSR for use in tape casting and 3D printing processes. This powder was subsequently pressed and sintered at 1150 °C to verify the phase-purity of the Ta-LLZO. The synthesized Ta-LLZO demonstrates a room-temperature ionic conductivity of 1.96 X 10^{-4} S cm^{-1}. Electrochemical test indicates that Ta-LLZO exhibits reasonable stability with metallic Li. This pre-sintered powder opens new possibilities for use as a source in the bulk tape casting and 3D printing processes, which may hold a significant importance for next-generation battery technology.

2. Materials and Methods

$Li_7La_3Zr_{1.6}Ta_{0.4}O_{12}$ was synthesized via solid-state reaction using La_2O_3 (95%, Merck, Germany), Li_2CO_3 (99%, Merck, Germany), Ta_2O_5 (99%, Merck, Germany), and monoclinic-ZrO_2 (Tosoh, Netherlands) as starting materials. To obtain 250 g of *c*-Ta-LLZO, 146.61 g of La_2O_3, 85.34 g of Li_2CO_3, 22.18 g of ZrO_2, and 26.51 g of Ta_2O_5, were planetary ball-milled (PM 400, Retsch GmbH, Germany). Here, the incorporation of Ta (0.4 mol) in the LLZO stabilizes the crystal structure of cubic-LLZO (c-LLZO) at room temperature [21]. Milling was performed at 300 rpm for 6 hours in ZrO_2 lined jars. The milling media consisted of 260 g ZrO_2 balls (3 mm diameter) and 2-propanol as the solvent. Addition of a 10% excess lithium source could compensate for lithium loss at elevated temperatures [13]. The slurry obtained from the milling process was dried at room temperature to remove the excess solvent. The mixed powder was die pressed at 100 MPa for one minute into 50 g pellets, which were then calcined at 950 °C for 6 hours in an Al_2O_3 crucible. The calcined pellets were ground manually using a mortar and pestle to achieve a homogeneous powder. The powder was uni-axially pressed into discs at 120 MPa held at this pressure for 5 minutes then removed and sintered at 1150 °C with a ramp rate of 3 °C/min for 1 hour in an MgO crucible with a closed lid, resulting in a high relatively dense, phase pure *c*-Ta-LLZO with disc dimensions of 0.7 mm thickness and 12 mm diameter. The schematic representation of the experimental section is shown in Figure S1.

Differential thermal analysis (DTA) and thermogravimetric analysis (TGA) were performed on wet-milled powders at a heating rate of 10 K/min in dynamic airflow (70 ml/min) using a STA-449 F3 Jupiter instrument (Netzsch GmbH & Co. KG, Germany). High temperature dilatometer DIL 402/E (Netzsch GmbH & Co. KG, Germany) with a pyrometer was used to measure the shrinkage of the Ta-LLZO disc under Argon atmosphere up to 1200°C. The phase formation of the disc was investigated using a PANalytical X'Pert powder diffractometer (Netherland). Rietveld refinement of X-ray diffraction patterns was performed using the FullProf software package [22]. To check for impurities in the Ta-LLZO discs, Raman spectra were collected using the confocal Raman spectroscopy device (WITec Alpha 300 R, Germany) with an excitation of 532 nm for thermally

doi:10.20944/preprints202310.1065.v1

treated pellets and discs. Additionally, X-ray photoelectron spectroscopy (XPS) measurements (Phi Quantum 2000) were performed. The densities of the sintered, *c*-Ta-LLZO discs were measured using the Archimedes method with 2-propanol. The density measurements were performed on at least two separate samples and the average value of density was reported. Scanning electron microscopy (SEM, Tascan Vega 3, Czech Republic) was performed on the wet-polished cross-section of both pellets and discs after sputtering with a thickness of 10 nm of Au/Pd alloy using a Leica EM ACE 200 sputter coater (Lecia, Germany). Symmetrical cell (Li|*c*-Ta-LLZO|Li) assembly and electrochemical characterization were performed under an argon atmosphere in a glovebox. Using a frequency response analyzer (FRA) (Solartron 1260A), the room temperature impedance of the pellets was measured to extract the resistance and conductivity values for the discs (0.7 mm x 12 mm diameter). The ion-conductivity of *c*-Ta-LLZO electrolyte was extracted from PEIS data measured at frequencies between 5 Hz and 25 MHz with a 20-mV sinusoidal amplitude. Electronic conductivity was determined by a DC polarization method (Mott–Schottky) at 1 V versus Li/Li^+ after 16 h stabilization using VMP-300 multi potentiostat (BioLogic, France). All electrochemical measurements were carried out in a Swagelok cell.

3. Results

3.1. Thermal analysis

The thermogravimetric analysis and dilatometry analysis were conducted to elucidate the weight loss and shrinkage behavior of Ta-LLZO from room temperature to 1200 °C. In Figure 1a, TG and DTA curves after wet milling of the Ta-LLZO powder are presented. The TG curve reveals four distinct weight loss steps and the corresponding endothermic peaks. The initial weight loss step (approximately to 300°C) is attributed to the presence of moisture and organic residues in the milled sample. The subsequent weight loss in the temperature range of 250 °C - 550 °C is associated with the transformation of $La(OH)_3$, formed during wet milling from La_2O_3. Wet milling of the oxide precursor, La_2O_3, leads to the formation of $La(OH)_3$ due to the topological transformation during the reaction process. This transformation is confirmed by the appearance of new peaks in the XRD spectra shown in Figure 1b and 1c. Moreover, during the milling process, mechanical activation can enhance the diffusion of dopant Ta into the LLZO lattice and concurrently can reduce the crystallinity of $LiCO_3$. This process improves the incorporation of Tantalum ions, thereby promoting stabilization of the cubic phase structure.

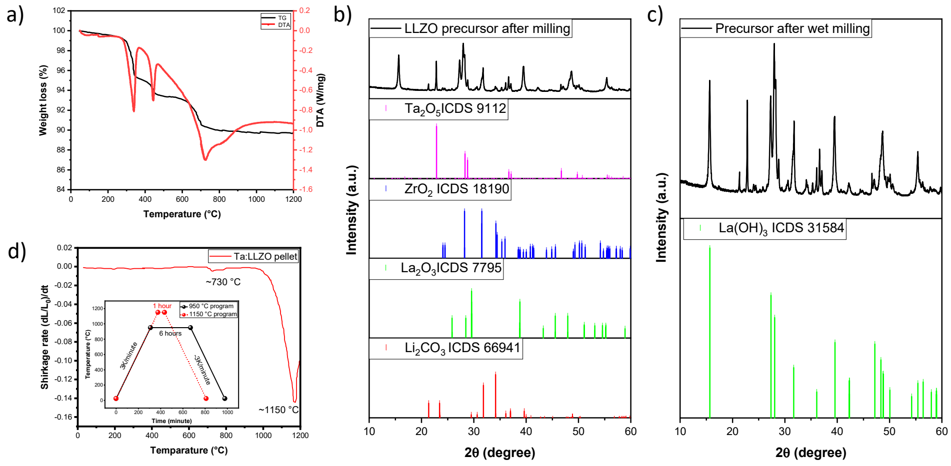

Figure 1. (a) TG/DTA analysis of Ta-LLZO precursor after wet milling process, (b) XRD patterns of wet milled powder and starting materials, (c) comparison of XRD patterns of reference $La(OH)_3$ (ICSD 31584) with wet milled powder and (d) constant heat rate dilatometry of Ta-LLZO conducted (RT–1200 °C) in an argon atmosphere (shrinkage rate as a function of temperature) and two step thermal process.

doi:10.20944/preprints202310.1065.v1

The TG/DTA curves for each individual starting material after milling are shown in Figure S2 (a-d). When comparing these TG/DTA curves with the first endothermic peak in the Figure 1(a), attributed to the formation of $La(OH)_3$ in the 250 to 550 °C range, it is evident that the next weight loss occurs in the region of 650 °C - 900 °C, corresponding to the decomposition of Li_2CO_3, which is in line with literature findings [23]. Above 900 °C, there is no weight loss up to 1200°C. Dilatometry measurements on Ta-LLZO pellets in the same temperature range, with a heating rate of 3 K/min (Figure 1d), reveal a small peak at 730 °C, indicating a slight shrinkage. Subsequently, after 1000°C, the main onset of densification and shrinkage behavior is observed, reaching completion at approximately 1150°C for Ta-LLZO.

3.2 *Phase analysis*

XRD patterns of Ta-LLZO after thermal processes at 950 °C (pellet) and 1150 °C (disc) are shown in Figure 2a. Following the 950 °C process, the cubic phase (*c*-LLZO) is observed in the Ta-LLZO powder, along with some impurity peaks representing tetragonal (*t*-LLZO), $La_2Zr_2O_7$, and Li_2CO_3. A strong diffraction peak at $2\theta=28.52°$, indicating the formation of $La_2Zr_2O_7$, is prominently visible. The tetragonal phase is confirmed by peaks at 2θ of 27.97, 47.42, 56.26, and 59.09 °. The presence of lithium carbonate is observed with weak diffraction peaks at 21.40, 31.85, 36.16, 37.05, and 39.49 °. Additionally, unidentified peaks at 29.92, 33.02, and 46.62 were also detected. The pellets achieved 73 % of relative density at 950 °C. Hence, a higher sintering temperature is required to obtain a phase pure and dense Ta-LLZO disc. According to dilatometry measurement, the Ta-LLZO samples were sintered at 1150 °C (Figure 1d). The peak intensity at 224 increases slightly with the 024 plane indicating the presence of Ta^{5+} ions in the LLZO crystal lattice. The ratio of 024/224 plane at 950 °C and 1150 °C is determined as 0.84 and 0.97, respectively. Here, the value of 0.97 that approaches to 1 indicates the presence of the cubic LLZO. Well-defined diffraction peaks perfectly match with cubic Ta-LLZO, indexed with the corresponding hkl planes without any impurity. According to Zhang et al. [24], a high intense peak was obtained at 33.83° (224) plane for cubic Ta-LLZO samples, and its intensity varies with respect to the concentration of Ta. In the presented XRD pattern (Figure 2a), a high-intensity peak was observed at 16.80° (112). Rangasamy et al. [2] reported that Al-LLZO shows a similar XRD pattern with a high-intensity peak at 16.80°. Additionally, alterations in lithium concentration, whether increased or decreased, could influence the phase of *c*-Ta-LLZO.

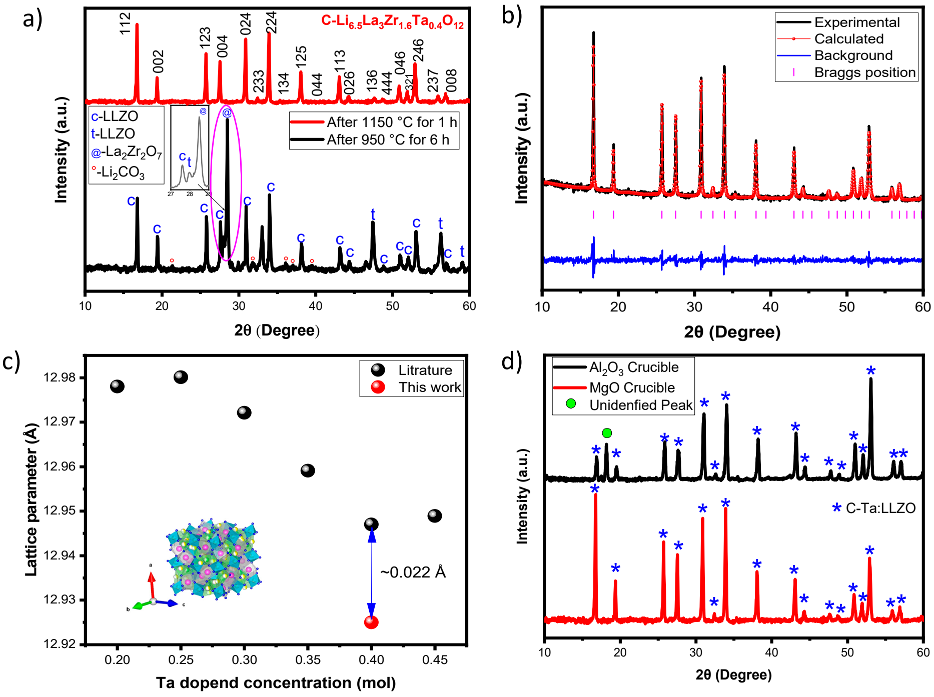

Figure 2. (a) XRD patterns of sample calcined at 950 °C (pellet) and 1150 °C (disc), (b) Rietveld refinement of *c*-Ta-LLZO disc after thermal processing at 1150 °C in MgO crucible, (c) lattice parameters as a function of Ta concentration, (d) XRD patterns of the prepared Ta-LLZO discs using Al_2O_3 or MgO crucibles after sintering at 1150 °C for 1 h.

Rietveld refinement was used to examine the lattice parameters of the aforementioned samples. The results of pattern fitting are shown in Figure 2b. The relative density after sintering the disc at 1150 °C is 96 % of the theoretical density, which is advantageous for electrochemical performance and will be discussed later. A comparison graph, plotting the cell parameter data extracted from the literature for different Ta-concentrations (Ta=0.2, 0.25, 0.30, 0.35, 0.40 and 0.45), is presented in Figure 2c. It is observed that an increase in Ta-content leads to a decrease in the lattice parameter [25,26]. The lattice parameter in this study is 12.944 Å similar to previous works with comparable Ta compositions [27–29].

Figure 2d illustrates the impact of the Al_2O_3 crucible in the high temperature sintering of Ta-LLZO discs. Notably, compared to discs sintered in an MgO crucible, those treated in an Al_2O_3 crucible exhibit a peak at 18.18°, which cannot be attributed to any other impurities of LLZO. Therefore, we designate this peak as an unidentified one, likely resulting from Al ions diffusing into LLZO structure at elevated temperatures exceeding 1000 °C. MgO crucibles were identified as suitable crucibles for obtaining dense phase pure cubic Ta-LLZO discs.

3.2 Vibration and elemental analysis

Raman spectroscopy was used to investigate the vibrational spectrum of the Ta-LLZO pellet (950 °C) and disc (1150 °C). In Figure 3a, all the peaks are indexed based on their vibrations in accordance with the literature [27–32]. The presence of the cubic phase has been confirmed by the existence of Li accommodating sites 24d (tetrahedral), and 96h (octahedral). In Figure 3a, in that specific region, the isolation of the peak is observed for the pellets (950 °C) whereas the discs (1150 °C) show a merged peak without any separation. This indicates the linkage of tetrahedral and octahedral regions contributing to Li movement in the crystal structure. This is a major reason why the cubic phase exhibits a higher ionic conductivity than the tetragonal phase [33].

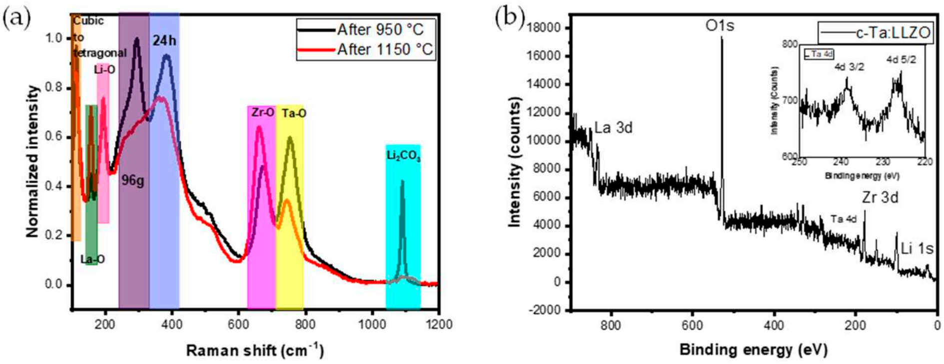

Figure 3. (a) Raman spectra of *c*-Ta-LLZO after heat treatment at 950 °C (pellet) and 1150 °C (disc), (b) X-ray photoelectron spectroscopy of *c*-Ta-LLZO after heat treatment at 1150 °C (inset-Ta 4d spectrum).

Raman spectroscopy was employed to investigate the aforementioned lithium accommodating site linkage. In line with this, the vibrations of Ta, Zr, Li, and La combined with oxygen vibrations were observed after heating cycles at 950°C (pellet) and 1150°C (disc). However, for pellets, the peaks appearing at 1090 cm^{-1} correspond to lithium carbonate. This lithium carbonate peak is consistent with the XRD pattern in Figure 2a. During the phase evaluation, no impurity peaks are identified for the dopant Ta. The presence of Ta is confirmed with the XPS analysis. XPS spectrum of *c*-Ta-LLZO is presented in Figure 3b, showing the peaks corresponding to the presence of La, O, Ta, Zr, and Li [34]. The inset in Figure 3b further depicts the presence of Ta.

doi:10.20944/preprints202310.1065.v1

3.4. Microstructural analysis

Microstructural analysis was performed to investigate the particle formation after heating to 950 °C (pellets) and 1150 °C (discs) using SEM. The morphology of the particles after 950 °C is observed to be agglomerated, as shown in Figure 4a. Notably, the morphology of the disc (1150 °C) reveals the absence of large holes and pores on the surface, with well interconnected grains, indicating good densification, as shown in Figure 4b. Additionally, the cross-section image of the disc in Figure 4c shows only a few small internal pores in the materials [35]. These characteristics are crucial for testing the samples for electrochemical measurements.

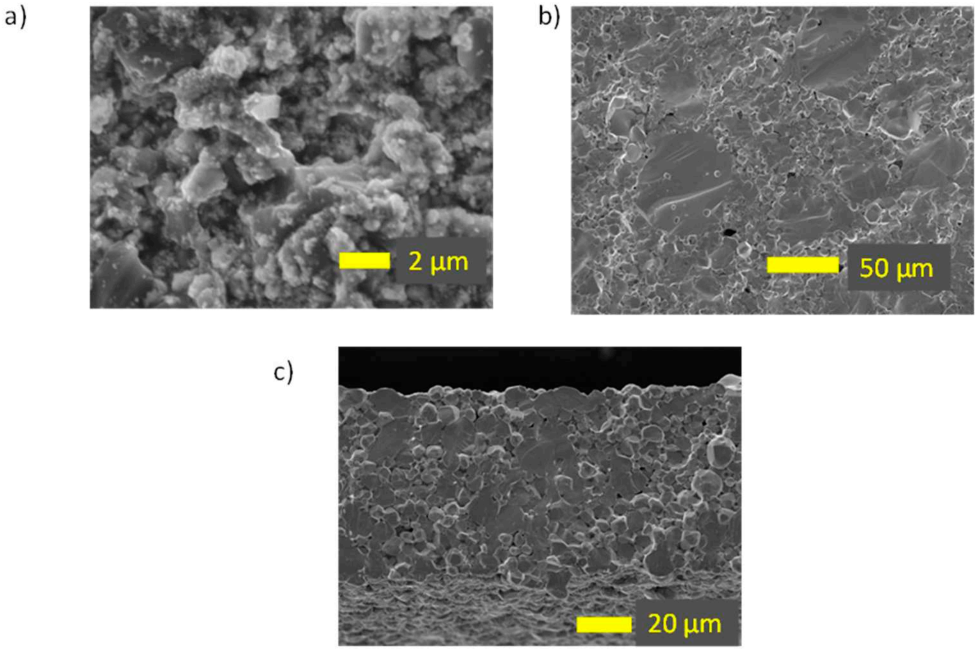

Figure 4. SEM microstructure image of *c*-Ta-LLZO (a) pellet (after 950 °C) (b) and (c) discs (1150 °C).

3.5. Electrochemical analysis

A solid electrolyte should exhibit ionic conductivity while remaining electronically insulating. In this study, the electronic and ionic conduction behaviors of *c*-Ta-LLZO discs were assessed. Electronic conductivity of the *c*-Ta-LLZO solid solution (Ta-doping) was investigated by using chronoamperometry measurements, applying a constant potential of 1V between Li||*c*-Ta-LLZO||Li configuration. Figure 5a shows the current as a function of time. Initially, the current exhibits a negative slope due to the polarization of the Ta-doped solid solution LLZO. The electronic conductivity was measured as 3.94 x 10^{-10} S cm^{-1} indicating insulating behavior of the solid electrolyte.

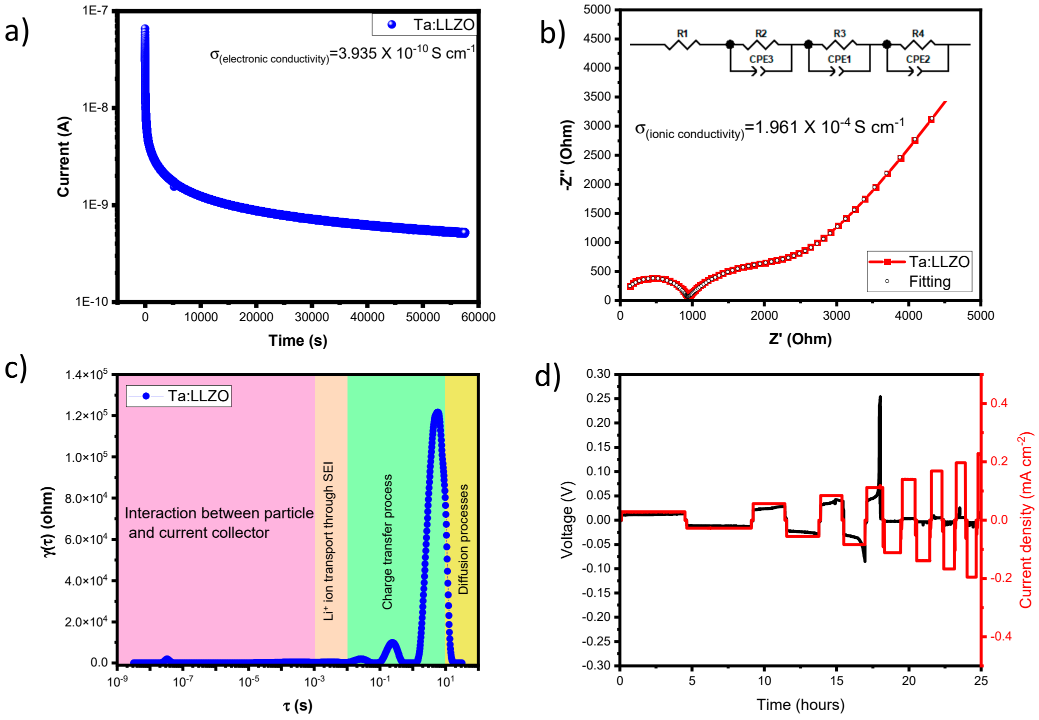

Figure 5. (a) Chronoamperometry measurement, (b) EIS measurement, (c) Differential Relaxation Time analysis and (d) Critical Current Density measurement of *c*-Ta-LLZO pellet.

Simultaneously, ionic conductivity was measured through electrochemical impedance spectroscopy (EIS) in the frequency range 24 MHz to 5 Hz. Figure 5b shows a spectrum with two semi-circles in the high and mid-frequency region and an inclined line in the low-frequency region in the Nyquist plot. The first semicircle represents the bulk boundary and the second represents the grain boundary [36]. The real axis in the Nyquist plot contributes to the total resistance. The observed two semi-circles and the addition of their individual resistance aligns with the real axis responsible for the total resistance. Fitting the spectrum using Z-view software provided the values for resistance, capacitance, and constant phase elements of the equivalent circuit (Figure 5b) and the ionic conductivity of the system is calculated as $1.96X10^{-4}$ S cm^{-1}. The Distribution of Relaxation Times (DRT) was employed for deconvoluting the EIS data to better understand the interactions of the different interfaces. [37–39]. Figure 5c shows peaks at different relaxation times, aiding in identification of interactions for charge transfer and diffusion process.

Finally, the critical current density measurement for *c*-Ta-LLZO is illustrated in Figure 5d. This measurement is crucial for identifying lithium dendrite formation during cell cycling at different current densities. It was reported that 0.3 to 0.7 mA cm^{-2} is the maximum limit for obtaining a good cyclability without polarization (lithium dendrite) [40,41]. However, *c*-Ta-LLZO shows better results at a current density of 0.09 mA cm^{-2} due to the absence of large voids. However, at 0.12 mA cm^{-2}, polarization is observed as shown in Figure 5d due to lithium penetration through the grain boundaries.

4. Conclusions

A cubic Ta-doped ($Li_7La_3Zr_{1.6}Ta_{0.4}O_{12}$) (*c*-Ta-LLZO) inorganic solid electrolyte was synthesized through a solid-state reaction. TG and DTA, and dilatometry analyses were employed to identify weight loss and densification of the material. The discs (sintered at 1150 °C) of *c*-Ta-LLZO exhibited a relative density of 96% without any large open pores on the surface or inside the structure.

The optimized synthesis process can be theoretically scaled up for larger industrial production, without alterations. Cells prepared from the sintered discs demonstrated promising electronic (3.94

X 10^{-10} S cm^{-1}) and ionic conductivity (1.96 X 10^{-4} S cm^{-1}) values, making them suitable as solid electrolytes for next generation solid state Li-ion batteries. Critical current density measurements indicated that *c*-Ta-LLZO performed well up to 0.09 mA cm^{-2}, but polarization was observed at a current density of 0.12 mA cm^{-2}, attributed to the growth of lithium dendrites via grain boundaries.

The synthesis process was optimized for laboratory-scale production, up to ~250 g of pre-sintered LLZO per batch. This powder is strongly recommended as a source for producing phase-pure *c*-Ta-LLZO using tape casting and 3D printing processes. Although, 250 g batch sizes were produced in this study, scaling up to several kg batches is feasible.

Supplementary Materials: The following supporting information can be downloaded at the website of this paper posted on Preprints.org. Figure S1: title; Table S1: title; Video S1: title.

Author Contributions: Conceptualization, G.B., T.G., F.C.; methodology, Y.L., D.Ka., D.Ko., A.H.; validation, N.S.Y, A.H.; formal analysis, D.Ka, D.Ko, N.S.Y., investigation, D.Ka, Y.L., P. V. W. S.; resources, G.B, T.G.; data curation, D.Ka, P.V. W.S.; writing—original draft preparation, D. Ka; writing—review and editing, G.B., N.S.Y.; visualization, N.S.Y., P.V.W. S.; supervision, G.B, F.C.; project administration, G.B.; funding acquisition, G.B., T.G.. All authors have read and agreed to the published version of the manuscript.

Funding: This work was partially funded by Innosuisse the Swiss Innovation Agency under project title “CAMELOT” funding agreement number 31236.1 IP-EE.

Acknowledgments: The authors would like to acknowledge the Swiss Innovation Agency-Innosuisse for funding this work as part of project 31236.1 IP-EE and Empa Internal Project Funding sources.

Conflicts of Interest: The authors declare no conflict of interest.

References

1. Shen, F.; Guo, W.; Zeng, D.; Sun, Z.; Gao, J.; Li, J.; Zhao, B.; He, B.; Han, X. A Simple and Highly Efficient Method toward High-Density Garnet-Type LLZTO Solid-State Electrolyte. *ACS Applied Materials & Interfaces* **2020**, *12*, 30313-30319, doi:10.1021/acsami.0c04850.
2. Rangasamy, E.; Wolfenstine, J.; Sakamoto, J. The role of Al and Li concentration on the formation of cubic garnet solid electrolyte of nominal composition Li7La3Zr2O12. *Solid State Ionics* **2012**, *206*, 28-32, doi:https://doi.org/10.1016/j.ssi.2011.10.022.
3. Buannic, L.; Orayech, B.; López Del Amo, J.-M.; Carrasco, J.; Katcho, N.A.; Aguesse, F.; Manalastas, W.; Zhang, W.; Kilner, J.; Llordés, A. Dual Substitution Strategy to Enhance Li+ Ionic Conductivity in Li7La3Zr2O12 Solid Electrolyte. *Chemistry of Materials* **2017**, *29*, 1769-1778, doi:10.1021/acs.chemmater.6b05369.
4. Xue, J.; Zhang, K.; Chen, D.; Zeng, J.; Luo, B. Spark plasma sintering plus heat-treatment of Ta-doped $Li_7La_3Zr_2O_{12}$ solid electrolyte and its ionic conductivity. *Materials Research Express* **2020**, *7*, 025518, doi:10.1088/2053-1591/ab7618.
5. Clemenceau, T.; Andriamady, N.; Kumar M.K, P.; Badran, A.; Avila, V.; Dahl, K.; Hopkins, M.; Vendrell, X.; Marshall, D.; Raj, R. Flash sintering of Li-ion conducting ceramic in a few seconds at 850 °C. *Scripta Materialia* **2019**, *172*, 1-5, doi:https://doi.org/10.1016/j.scriptamat.2019.06.038.
6. Zhang, Y.; Chen, F.; Tu, R.; Shen, Q.; Zhang, L. Field assisted sintering of dense Al-substituted cubic phase $Li_7La_3Zr_2O_{12}$ solid electrolytes. *Journal of Power Sources* **2014**, *268*, 960-964, doi:https://doi.org/10.1016/j.jpowsour.2014.03.148.
7. Li, H.-Y.; Huang, B.; Huang, Z.; Wang, C.-A. Enhanced mechanical strength and ionic conductivity of LLZO solid electrolytes by oscillatory pressure sintering. *Ceramics International* **2019**, *45*, 18115-18118, doi:https://doi.org/10.1016/j.ceramint.2019.05.241.
8. Yang, L.; Dai, Q.; Liu, L.; Shao, D.; Luo, K.; Jamil, S.; Liu, H.; Luo, Z.; Chang, B.; Wang, X. Rapid sintering method for highly conductive $Li_7La_3Zr_2O_{12}$ ceramic electrolyte. *Ceramics International* **2020**, *46*, 10917-10924, doi:https://doi.org/10.1016/j.ceramint.2020.01.106.
9. Kravchyk, K.V.; Karabay, D.T.; Kovalenko, M.V. On the feasibility of all-solid-state batteries with LLZO as a single electrolyte. *Scientific Reports* **2022**, *12*, 1177, doi:10.1038/s41598-022-05141-x.
10. Xiang, X.; Chen, F.; Shen, Q.; Zhang, L.; Chen, C. Effect of the lithium ion concentration on the lithium ion conductivity of Ga-doped LLZO. *Materials Research Express* **2019**, *6*, 085546, doi:10.1088/2053-1591/ab2799.

11. Yi, E.; Wang, W.; Kieffer, J.; Laine, R.M. Flame made nanoparticles permit processing of dense, flexible, Li^+ conducting ceramic electrolyte thin films of cubic-$Li_7La_3Zr_2O_{12}$ (*c*-LLZO). *Journal of Materials Chemistry A* **2016**, *4*, 12947-12954, doi:10.1039/C6TA04492A.
12. Badami, P.; Smetaczek, S.; Limbeck, A.; Rettenwander, D.; Chan, C.K.; Kannan, A.N.M. Facile synthesis of Al-stabilized lithium garnets by a solution-combustion technique for all solid-state batteries. *Materials Advances* **2021**, *2*, 5181-5188, doi:10.1039/D1MA00393C.
13. Jiang, Y.; Zhou, Y.; Hu, Z.; Huang, Y.; Zhu, X. MgO or Al_2O_3 crucible: Which is better for the preparation of LLZ-based solid electrolytes? *Ceramics International* **2020**, *46*, 3367-3373, doi:https://doi.org/10.1016/j.ceramint.2019.10.046.
14. Cao, Y.; Li, Y.-Q.; Guo, X.-X. Densification and lithium ion conductivity of garnet-type $Li_7La_3Zr_{2-x}Ta_xO_{12}$(x= 0.25) solid electrolytes. *Chinese Physics B* **2013**, *22*, 078201, doi:10.1088/1674-1056/22/7/078201.
15. Weller, J.M.; Whetten, J.A.; Chan, C.K. Synthesis of fine cubic $Li_7La_3Zr_2O_{12}$ powders in molten LiCl–KCl eutectic and facile densification by reversal of Li^+/H^+ exchange. *ACS Applied Energy Materials* **2018**, *1*, 552-560, doi:10.1021/acsaem.7b00133.
16. Xia, W.; Xu, B.; Duan, H.; Guo, Y.; Kang, H.; Li, H.; Liu, H. Ionic conductivity and air stability of Al-doped $Li_7La_3Zr_2O_{12}$ sintered in alumina and Pt crucibles. *ACS Applied Materials & Interfaces* **2016**, *8*, 5335-5342, doi:10.1021/acsami.5b12186.
17. Huang, X.; Lu, Y.; Guo, H.; Song, Z.; Xiu, T.; Badding, M.E.; Wen, Z. None-mother-powder method to prepare dense Li-garnet solid electrolytes with high critical current density. *ACS Applied Energy Materials* **2018**, *1*, 5355-5365, doi:10.1021/acsaem.8b00976.
18. Sato, M.; Garcia-Mendez, R.; Sakamoto, J. Mapping hot-pressed $Li_{6.25}Al_{0.25}La_3Zr_2O_{12}$ (LLZO) grains and grain boundaries through a simple thermal grooving technique. *Journal of Asian Ceramic Societies* **2020**, *8*, 793-803, doi:10.1080/21870764.2020.1789286.
19. Cheng, L.; Wu, C.H.; Jarry, A.; Chen, W.; Ye, Y.; Zhu, J.; Kostecki, R.; Persson, K.; Guo, J.; Salmeron, M.; et al. Interrelationships among grain size, surface composition, air stability, and interfacial resistance of Al-substituted $Li_7La_3Zr_2O_{12}$ solid electrolytes. *ACS Applied Materials & Interfaces* **2015**, *7*, 17649-17655, doi:10.1021/acsami.5b02528.
20. Heo, T.W.; Grieder, A.; Wang, B.; Wood, M.; Hsu, T.; Akhade, S.A.; Wan, L.F.; Chen, L.-Q.; Adelstein, N.; Wood, B.C. Microstructural impacts on ionic conductivity of oxide solid electrolytes from a combined atomistic-mesoscale approach. *npj Computational Materials* **2021**, *7*, 214, doi:10.1038/s41524-021-00681-8.
21. Inada, R.; Takeda, A.; Yamazaki, Y.; Miyake, S.; Sakurai, Y.; Thangadurai, V. Effect of postannealing on the properties of a Ta-doped $Li_7La_3Zr_2O_{12}$ solid electrolyte degraded by Li dendrite penetration. *ACS Applied Energy Materials* **2020**, *3*, 12517-12524, doi:10.1021/acsaem.0c02474.
22. Fritsch, C.; Zinkevich, T.; Indris, S.; Etter, M.; Baran, V.; Bergfeldt, T.; Knapp, M.; Ehrenberg, H.; Hansen, A.-L. Garnet to hydrogarnet: effect of post synthesis treatment on cation substituted LLZO solid electrolyte and its effect on Li ion conductivity. *RSC Advances* **2021**, *11*, 30283-30294, doi:10.1039/D1RA05961K.
23. Huang, Z.; Liu, K.; Chen, L.; Lu, Y.; Li, Y.; Wang, C.-A. Sintering behavior of garnet-type $Li_{6.4}La_3Zr_{1.4}Ta_{0.6}O_{12}$ in Li_2CO_3 atmosphere and its electrochemical property. *International Journal of Applied Ceramic Technology* **2017**, *14*, 921-927, doi:https://doi.org/10.1111/ijac.12735.
24. Zhang, Y.; Deng, J.; Hu, D.; Chen, F.; Shen, Q.; Zhang, L.; Dong, S. Synergistic regulation of garnet-type Ta-doped $Li_7La_3Zr_2O_{12}$ solid electrolyte by Li^+ concentration and Li^+ transport channel size. *Electrochimica Acta* **2019**, *296*, 823-829, doi:https://doi.org/10.1016/j.electacta.2018.11.136.
25. Yi, M.; Liu, T.; Wang, X.; Li, J.; Wang, C.; Mo, Y. High densification and Li-ion conductivity of Al-free $Li_{7-x}La_3Zr_{2-x}Ta_xO_{12}$ garnet solid electrolyte prepared by using ultrafine powders. *Ceramics International* **2019**, *45*, 786-792, doi:https://doi.org/10.1016/j.ceramint.2018.09.245.
26. Ramakumar, S.; Deviannapoorani, C.; Dhivya, L.; Shankar, L.S.; Murugan, R. Lithium garnets: Synthesis, structure, Li^+ conductivity, Li^+ dynamics and applications. *Progress in Materials Science* **2017**, *88*, 325-411, doi:https://doi.org/10.1016/j.pmatsci.2017.04.007.
27. Gajraj, V.; Kumar, A.; Indris, S.; Ehrenberg, H.; Kumar, N.; Mariappan, C.R. Influence of Al on the structure and ion transport in garnet-type $Li_7La_{3-x}Al_xZr_2O_{12}$ solid electrolytes for Li-ion batteries. *Ceramics International* **2022**, doi:https://doi.org/10.1016/j.ceramint.2022.05.199.
28. Gonzalez Puente, P.M.; Song, S.; Cao, S.; Rannalter, L.Z.; Pan, Z.; Xiang, X.; Shen, Q.; Chen, F. Garnet-type solid electrolyte: Advances of ionic transport performance and its application in all-solid-state batteries. *Journal of Advanced Ceramics* **2021**, *10*, 933-972, doi:10.1007/s40145-021-0489-7.

29. Larraz, G.; Orera, A.; Sanjuán, M.L. Cubic phases of garnet-type $Li_7La_3Zr_2O_{12}$: the role of hydration. *Journal of Materials Chemistry A* **2013**, *1*, 11419-11428, doi:10.1039/C3TA11996C.
30. Hirose, E.; Niwa, K.; Kataoka, K.; Akimoto, J.; Hasegawa, M. Structural stability of the Li-ion conductor $Li_7La_3Zr_2O_{12}$ investigated by high-pressure in-situ X-ray diffraction and Raman spectroscopy. *Materials Research Bulletin* **2018**, *107*, 361-365, doi:https://doi.org/10.1016/j.materresbull.2018.07.034.
31. Rettenwander, D.; Welzl, A.; Cheng, L.; Fleig, J.; Musso, M.; Suard, E.; Doeff, M.M.; Redhammer, G.J.; Amthauer, G. Synthesis, crystal chemistry, and electrochemical properties of $Li_{7-2x}La_3Zr_{2-x}Mo_xO_{12}$ (x=0.1–0.4): stabilization of the cubic garnet polymorph via substitution of Zr^{4+} by Mo^{6+}. *Inorganic Chemistry* **2015**, *54*, 10440-10449, doi:10.1021/acs.inorgchem.5b01895.
32. Sharafi, A.; Yu, S.; Naguib, M.; Lee, M.; Ma, C.; Meyer, H.M.; Nanda, J.; Chi, M.; Siegel, D.J.; Sakamoto, J. Impact of air exposure and surface chemistry on Li–$Li_7La_3Zr_2O_{12}$ interfacial resistance. *Journal of Materials Chemistry A* **2017**, *5*, 13475-13487, doi:10.1039/C7TA03162A.
33. Rustad, J.R. The effect of tetrahedral versus octahedral network-blocking atom substitutions on lithium ion conduction in LLZO garnet. *arXiv preprint arXiv:1605.08598* **2016**.
34. Zhu, Y.; Connell, J.G.; Tepavcevic, S.; Zapol, P.; Garcia-Mendez, R.; Taylor, N.J.; Sakamoto, J.; Ingram, B.J.; Curtiss, L.A.; Freeland, J.W.; et al. Dopant-dependent stability of garnet solid electrolyte interfaces with lithium metal. *Advanced Energy Materials* **2019**, *9*, 1803440, doi:https://doi.org/10.1002/aenm.201803440.
35. Huang, X.; Lu, Y.; Song, Z.; Rui, K.; Wang, Q.; Xiu, T.; Badding, M.E.; Wen, Z. Manipulating Li_2O atmosphere for sintering dense $Li_7La_3Zr_2O_{12}$ solid electrolyte. *Energy Storage Materials* **2019**, *22*, 207-217, doi:https://doi.org/10.1016/j.ensm.2019.01.018.
36. Deng, Y.-F.; Zhao, S.-X.; Xu, Y.-H.; Nan, C.-W. Effect of the morphology of Li–La–Zr–O solid electrolyte coating on the electrochemical performance of spinel $LiMn_{1.95}Ni_{0.05}O_{3.98}F_{0.02}$ cathode materials. *Journal of Materials Chemistry A* **2014**, *2*, 18889-18897, doi:10.1039/C4TA03772C.
37. Hahn, M.; Rosenbach, D.; Krimalowski, A.; Nazarenus, T.; Moos, R.; Thelakkat, M.; Danzer, M.A. Investigating solid polymer and ceramic electrolytes for lithium-ion batteries by means of an extended Distribution of Relaxation Times analysis. *Electrochimica Acta* **2020**, *344*, 136060, doi:https://doi.org/10.1016/j.electacta.2020.136060.
38. Chen, X.; Li, L.; Liu, M.; Huang, T.; Yu, A. Detection of lithium plating in lithium-ion batteries by distribution of relaxation times. *Journal of Power Sources* **2021**, *496*, 229867, doi:https://doi.org/10.1016/j.jpowsour.2021.229867.
39. Iurilli, P.; Brivio, C.; Carrillo, R.E.; Wood, V. EIS2MOD: A DRT-based modeling framework for li-ion cells. *IEEE Transactions on Industry Applications* **2021**, *58*, 1429-1439.
40. Flatscher, F.; Philipp, M.; Ganschow, S.; Wilkening, H.M.R.; Rettenwander, D. The natural critical current density limit for $Li_7La_3Zr_2O_{12}$ garnets. *Journal of Materials Chemistry A* **2020**, *8*, 15782-15788, doi:10.1039/C9TA14177D.
41. Jiang, W.; Dong, L.; Liu, S.; Ai, B.; Zhao, S.; Zhang, W.; Pan, K.; Zhang, L. Improvement of the interface between the lithium anode and a garnet-type solid electrolyte of lithium batteries using an aluminum-nitride layer. *Nanomaterials* **2022**, *12*, 2023.